Solution structure of a europium-nicotianamine complex supports that phytosiderophores bind lanthanides

Danil S. Kaliakin[1], Jorge H.S.K. Monteiro[2], Ana de Bettencourt-Dias[2], David C. Cantu[1*]

[1]*Chemical and Materials Engineering Department,* [2]*Chemistry Department, University of Nevada, Reno*

[*]*Corresponding author: E-mail: dcantu@unr.edu*

Phone: +1 775-784-1792

ABSTRACT

We report the solution structure of a europium-nicotianamine complex predicted from ab initio molecular dynamics simulations with density functional theory. Emission and excitation spectroscopy measurements show that the Eu^{3+} coordination environment changes in the presence of nicotianamine, suggesting complex formation, and strongly supporting the predicted Eu^{3+}-nicotianamine complex structure from computation. We used our recently optimized pseudopotentials and basis sets for lanthanides to model Eu^{3+}-ligand complexes with explicit water molecules in periodic boxes, effectively simulating the solution phase. Our simulations consider possible chemical events (e.g. coordination bond formation, protonation state changes, charge transfers), as well as ligand flexibility and solvent rearrangements. Our computational approach correctly predicts the solution structure of a Eu^{3+}-ethylenediaminetetraacetic acid complex within 0.05 Å of experimentally measured values, backing the fidelity of the predicted solution structure of the Eu^{3+}-nicotianamine complex. Emission and excitation spectroscopy measurements were also performed on the well-known Eu^{3+}-ethylenediaminetetraacetic acid complex to validate our experimental methods. The electronic structure of the Eu^{3+}-nicotianamine complex is analyzed to describe electron densities and coordination bonds in greater detail. Nicotianamine is a metabolic precursor of, and structurally very similar to, phytosiderophores, which are responsible for the uptake of metals in plants. Although knowledge that nicotianamine binds europium does not determine how plants uptake rare earths from the environment, it strongly supports that phytosiderophores bind lanthanides.

I. Introduction

The remarkable and unique characteristics of electronic states of lanthanide (Ln) complexes originating from partially filled 4*f*-electron shells, and their extremely localized nature, make studies of their compounds a very active area of research.[1–10] Ln complexes are used in a multitude of high-tech applications.[11] At the same time, the role of lanthanides in naturally occurring biological systems was somewhat overlooked. Until recently, lanthanides were not considered as essential elements of biological systems and Ln-incorporated enzymes were viewed as useful, yet mainly artificial, systems.[11–13] This perspective changed with the discovery of lanthanides in bacterial methanol dehydrogenases.[14–16] Moreover, a number of studies show that the Ln elements, especially Ce, affect the growth and development of agriculturally important crops.[17,18] However, currently there is no certainty regarding Ln intake pathways and accumulation in plants. It is not clear whether accumulation happens through Ca or Fe uptake pathways involving the broad-spectrum metallophore nicotianamine (NA), or if Ln intake and accumulation are the result of production of lanthanophores by bacteria residing in the phyllosphere.[12,19]

Low-molecular weight chelators with functional carboxy-, amino- and hydroxy-groups facilitating metal coordination in bacteria and plants are classified as siderophores and phytosiderophores, respectively.[20–23] When it comes to understanding the role of these compounds in the metabolism of lanthanides in plants, NA, a metallophore naturally occurring in higher plants,[20,24] is of particular interest. NA is structurally very similar to phytosiderophores, and it is a precursor in phytosiderophores biosynthetic pathways,[20] which makes it an ideal model system.

Apart from its importance for understanding the role of lanthanides in plant of metabolic transformations, elucidating the solution structure of Ln^{3+} complexes with NA could potentially contribute to the development of novel ligands for Ln extraction. Phytosiderophores are polydentate and polyacidic, with a wide range of p*K*a sites, therefore solution pH changes the protonation state of each acidic site, impacting the Ln coordination structure. It is well known that changes in solution acidity facilitates Ln extraction, additionally, recent studies with europium,[25] gadolinium,[26] and terbium[27] demonstrate how solution pH affects Ln complex coordination structures and their surrounding environment. Moreover, previous studies show that tuning the flexibility of polydentate and polyacidic ligands is well suited for Ln separations,[28,29]

highlighting the importance of ligand flexibility. Siderophores have been shown to bind Ln^{3+} ions[30–32] with a pH-sensitive binding behavior.[31,33] Like siderophores, the molecular structures of phytosiderophores are highly susceptible to changes in protonation states,[20,34–36] but, unlike siderophores, their ability to bind Ln^{3+} ions has not been elucidated. Although lanthanides have been detected in plants and their roots,[17–19,37] and uptake mechanisms of other trivalent elements were previously reported,[38] apart from few hypotheses, the plant uptake mechanisms of Ln^{3+} remains largely unknown.[19,39]. Interestingly, Liu et al.[40] demonstrated that Rubisco,[41] an enzyme crucial for photosynthetic CO_2 fixation in higher plants,[40,42] binds cerium, which demonstrates Ln^{3+}-binding capability of compounds native to plants. To date, there are no reported *in vitro* or *in silico* studies of Ln ions and phytosiderophores.

Lanthanide coordination is affected by a number of factors in the coordination environment, such as flexibility and protonation state of the bound ligand.[43–46] Due to the high coordination number of Ln^{3+} ions, in addition to the ligand, water (or solvent) molecules will coordinate as well. Thus, the solution structure of Ln^{3+}-ligand complexes and their stabilities strongly depend on the molecular structure of their coordination spheres, which include ligand and solvent molecules.[47]

Resolving the solution structure of Ln^{3+}-ligand complexes is a nontrivial task due to their highly dynamical nature in solution. To do so computationally in atomic resolution requires the use of density functional theory (DFT) and ab initio molecular dynamics (AIMD) simulations to simulate the breakage and formation of chemical bonds (e.g. coordination bonds, protonation state changes) simultaneously considering ligand flexibility and solvent rearrangements. Additionally, simulating solution structures (i.e. condensed phase) requires including explicit solvent molecules, and treating the system periodically in repeating unit cells. An accurate periodic treatment of solute-solvent systems requires periodic boxes of sufficient size, which makes such all-electron AIMD simulations computationally out of reach, thus requiring DFT.

The employment of relativistic, norm-conserving, separable, dual-space Gaussian-type pseudopotential protocol of Goedecker, Teter, and Hutter (GTH)[48–50] in a mixed Gaussian−plane wave scheme[51] has proved to be an effective and efficient way to perform AIMD simulations of larger systems (> 500 atoms)[52,53] and with longer trajectories (> 10 ps),[52,54] significantly reducing the computational cost of such simulations. Until recently, accurate GTH pseudopotentials and basis sets for the lanthanides, besides cerium,[55,56] were lacking. This prevented performing

larger-scale DFT and AIMD simulations of lanthanide-containing systems in the condensed phase or solid state. Our previous work bridged this critical gap by producing LnPP1: a full set of well-benchmarked pseudopotentials along with the corresponding basis sets within GTH protocol specifically optimized for GGA PBE[57] calculations of lanthanide-containing systems.[58] Despite the fact that other types of lanthanide pseudopotentials (i.e. effective core potentials) and basis sets were previously reported,[59–65] these were employed in electronic structure calculations with lanthanide systems containing less than ~100 atoms.[66,67] Thus, simulating the solution structure of lanthanide-ligand complexes, with molecular dynamics sampling to explicitly include solvent rearrangement and ligand flexibility, was not possible until very recently. Our LnPP1 complete set of pseudopotentials and accompanying basis sets enabled us to perform DFT calculations and AIMD simulations of lanthanide-ligand complexes in explicit water boxes in periodic conditions (system > 500 atoms) in the present paper.

This work pursued two goals: i) demonstrate that our pseudopotentials and basis sets (LnPP1) with AIMD simulations can predict the structures of lanthanide complexes in solution and, ii) elucidate the molecular and electronic structure of Eu^{3+}-nicotianamine complexes in aqueous solution. Our previous work[58] demonstrated the accuracy of our LnPP1 pseudopotentials and basis sets to replicate Ln reactivity (e.g. oxidation reactions, heats of formation, ionization potentials). This work shows that our pseudopotentials and basis sets with AIMD simulations replicate the solution structure of lanthanide-ligand complexes, by correctly (within 0.05 Å) predicting the structure of a complex whose structure is known (Eu^{3+}-ethylenediaminetetraacetic acid [EDTA]).[68,69] Upon validation of the computational approach, we predict the structure of Eu^{3+}-nicotianamine complexes in solution: this work describes their molecular structures (e.g. ligand conformation, water molecule inclusion, coordination bond geometry) and electronic structure (e.g. molecular orbitals, electron densities). Further, with excitation and emission spectroscopy, we measured an *in vitro* change in Eu^{3+} coordination upon coming in contact with nicotianamine, supporting the formation of a Eu^{3+}-nicotianamine complex.

II. Methods

II.A. Computational Details

<u>II.A.1. Ab initio molecular dynamics simulations</u>

All geometry optimizations and AIMD simulations were performed in 17.5 Å cubic periodic boxes within the PBE/LnPP1 GTH level of theory as implemented in the CP2K computational chemistry software package.[70] Core electrons were modeled with norm-conserving GTH pseudopotentials, while valence electrons including *f* electrons, were treated with polarizable double-zeta quality basis sets.[71] We used our recently developed LnPP1 pseudopotentials and basis sets for europium.[58] The long-range electrostatics terms were calculated with an additional plane wave basis set with a 500 Ry cutoff. Grimme's corrections[72] were used to account for van der Waals interactions with a 6.0 Å radius.

All AIMD simulations were done in the NVT ensemble, with a 1.0 fs or 0.5 fs time step. A 1.0 fs time step is sufficient, although initially we used a 0.5 fs time step. Initial complex structures were placed in the center of the periodic box and solvated with water molecules. We used the following protocol to obtain optimized aqueous structures of the Eu^{3+}-ligand complexes: we initially performed 5 ps of NVT AIMD simulations at 363 K, which were followed by a slow annealing to 0 K with rescaling factor for annealing velocities equal to 0.997, and final geometries optimizations. Starting from the optimized geometries, production AIMD simulations of Eu^{3+}-ligand complexes were performed at 300 K for >10 ps trajectories. The analysis of radial distribution functions (RDFs) and coordination numbers (CNs) of the studied systems was done for equilibrated parts of the trajectories that corresponded to at least ~10 ps. Potential energy plots along the production AIMD trajectories appear in the Supporting Information (SI), Figure S1. All of the models containing Eu^{3+} had a septet spin multiplicity.

We modelled the Eu^{3+}-EDTA complex with the EDTA protonation state corresponding to pH 11 (four carboxylate sites and two amine sites deprotonated) resulting in $EDTA^{4-}$. The EDTA protonation states were chosen to correspond to pH 11 so to be able to directly compare with the published Eu^{3+}-EDTA complex structure.[68,69] Our model periodic unit cell contained 574 atoms, which included 33 atoms representing the $[Eu^{3+}\text{-}EDTA^{4-}]^{-}$ complex, 180 explicit water molecules, and 1 Na^{+} counter ion, allowing for the overall neutral charge of the periodic unit cell (Figure 1a). Since the structure of the $[Eu^{3+}\text{-}EDTA^{4-}]^{-}$ complex in solution is known, we initially constructed the complex with the known structure, and subjected it to the AIMD protocol described.

We modelled the Eu^{3+}-NA complex with NA as a zwitterion (three carboxylate sites deprotonated and three amine sites protonated) resulting in a net uncharged ligand. NA has a

zwitterionic protonation state from pH ~3.2 to pH ~7.7.[20,73] We modelled NA as a zwitterion to directly compare with our experiments performed at pH ~5. Our model periodic unit cell contained 586 atoms, which included 43 atoms corresponding to the $[Eu^{3+}\text{-NA}]^{3+}$ complex, 180 explicit water molecules, and three Cl^- counter ions allowing for the overall neutral charge of the unit cell (Figure 1b). Because we did not know *a priori* the $[Eu^{3+}\text{-NA}]^{3+}$ complex structure, and in order to account for different possible conformations, we independently constructed this system with three different initial structures: i) structure with all three NA-COO^- groups having bidentate binding to Eu^{3+}, ii) structure with two bidentate NA-COO^- groups binding to Eu^{3+} and one monodentate and iii) structure with one bidentate NA-COO^- group and two monodentate. All three initial structures were independently subjected to the AIMD protocol described. Due to the large number of degrees of freedom in explicitly solvated $[Eu^{3+}\text{-NA}]^{3+}$ complexes, we performed additional ~4ps AIMD simulations at 500 K, to verify their stabilities.

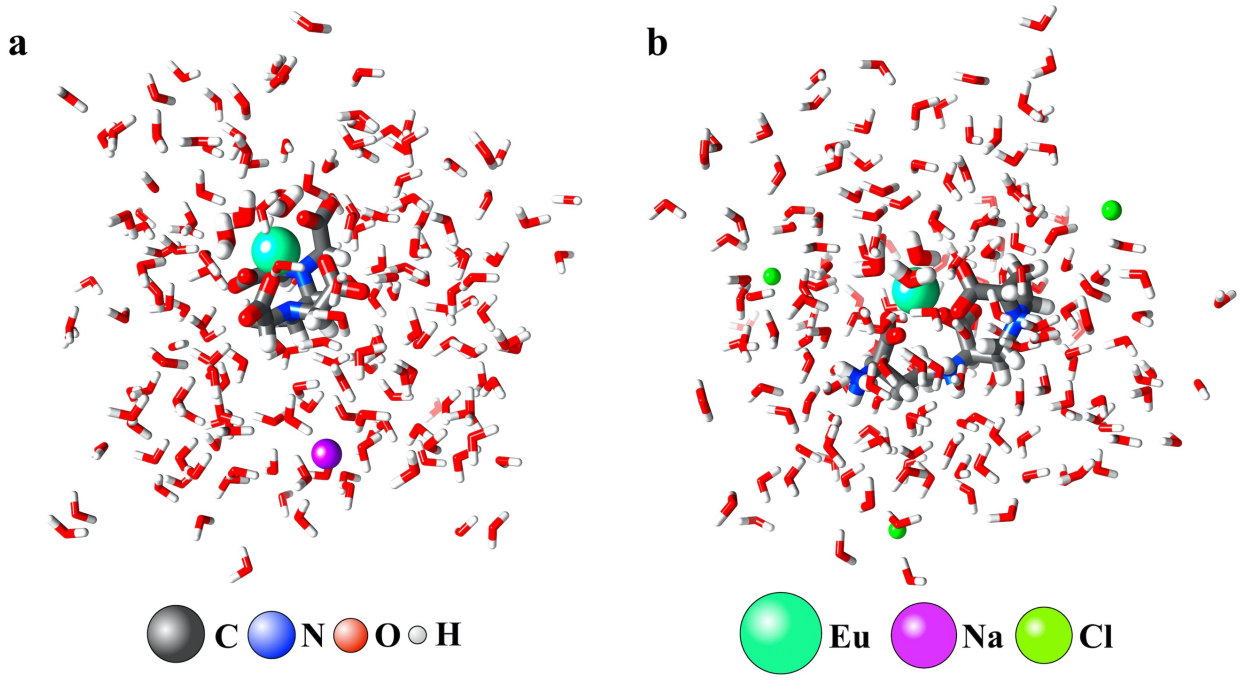

Figure 1. Unit cells used in periodic simulations. a) Unit cell of the Eu^{3+}-$EDTA^{4-}$ model system. b) Unit cell of the Eu^{3+}-NA model system.

II.A.2. Electronic structure analysis

We studied the electronic structure of the optimized complex structures in further detail by: i) examining how the electron density changes between the bound Eu^{3+}-ligand complex and

unbound Eu^{3+} ion and ligand, and ii) analyzing the molecular orbitals (MOs) of the Eu^{3+}-ligand complex coordination bonds. Starting from the optimized (annealing plus geometry optimization) solution structures of our Eu^{3+}-ligand complexes with explicit water molecules, we extracted the atomic coordinates of the Eu^{3+}-ligand complexes, including water molecules that are directly coordinated with the Eu^{3+} ion, and performed single point energy calculations in the Gaussian software package[74] with PBE functional,[57] ECP28MWBSEG basis set with corresponding effective core potential for Eu,[64,75] and cc-pVTZ basis set for other chemical elements within the model systems.[76] All single point energy calculations were done with polarizable continuum model implicit water solvent.[77–80]

All geometry optimizations were done in the solution phase (i.e. with explicit water molecules, periodic conditions) with CP2K, and we extracted the coordinates of only the molecules (ligand and water) coordinated with Eu^{3+} ions to analyze the electronic structure of the complexes. We did not further optimize the structures with implicit solvent to directly probe the electronic properties of the structures resolved with DFT and AIMD in aqueous solution.

For each complex, we examined how the electron density changes between the formed Eu^{3+}-ligand complexes (including coordinated water molecules) and their unbound ligand, coordinated water molecules, and Eu^{3+} ion. This was done through subtraction of electronic densities[81] of the bound and unbound states, as represented by equation 1.

$$\Delta\rho = \rho_{complex} - (\rho_{[ligand+water]} + \rho_{Eu^{3+}}) \quad (1)$$

Where $\Delta\rho$ is the change in electronic density upon binding, $\rho_{complex}$ is the electron density of the Eu^{3+}-ligand complexes, $\rho_{[ligand+water]}$ is the electron density of the ligand and coordinated water molecules, and $\rho_{Eu^{3+}}$ is the electron density of the Eu^{3+} ion. Also, we analyzed the valence MOs of these complexes and classified them based on the dominant contributions of ligands forming given MOs.

II.B. Experimental Details

II.B.1. Complex and solution preparation

$EuCl_3 \cdot (H_2O)_6$ was purchased from Strem Chemicals and dried under reduced pressure and heating for at least 12 hours. NA was purchased from Toronto Research Chemicals and, like all other reagents, used as received. Solvents were dried by standard methods. NA was dissolved in

water and deprotonated with 3 equivalents of NaOH(aq). The pH of the NA solution was ~5.5. Dry $EuCl_3$ dissolved in H_2O was added in a 1:1 stoichiometry. The pH decreased to ~4.8. No precipitation was observed. Solutions with concentrations 1×10^{-4} M were prepared for photophysical studies.

We prepared Eu^{3+}-EDTA complexes to verify our experimental methods and support our results with Eu^{3+}-NA complexes. Eu^{3+}-EDTA complexes were formed by mixing Na_2-EDTA and dry $EuCl_3$ in a 1:1 stoichiometry in water. The pH was adjusted to ~2.9, with HCl(aq), or pH ~7.1, with $Na_2HPO_4/NaHPO_4$ buffer. At pH ~2.9 the resulting complex is $[Eu^{3+}\text{-}EDTA^{2-}\cdot(H_2O)_n]^+$ complex, and at pH ~7.1 it is $[Eu^{3+}\text{-}EDTA^{3-}\cdot(H_2O)_n]$.

II.B.2. Photophysical studies

The photoluminescence data were obtained on a Fluorolog-3 spectrofluorimeter (Horiba FL3-22-iHR550), with a 1200 grooves/mm excitation monochromator with gratings blazed at 330 nm and a 1200 grooves/mm emission monochromator with gratings blazed at 500 nm. An ozone-free 450 W xenon lamp (Ushio) was used as a radiation source. The emission spectra were measured in the range 550-725 nm using a Hamamatsu 928P detector. All emission spectra were corrected for instrumental function. The emission decay curves were obtained using a Horiba TCSPC system and a Xe pulsed lamp as the excitation source.

The number of coordinated water molecules (q) was obtained by measuring the emission decay lifetimes in water and D_2O and equation 2.[82]

$$q = 1.1 \times \left(\frac{1}{\tau_{H2O}} - \frac{1}{\tau_{D2O}} - 0.31\right) \qquad (2)$$

All photophysical measurements are the average of at least three independent measurements, and, unless otherwise indicated, performed at 25.0 ± 0.1°C.

III. Results and Discussion

III.A. Our computational approach replicates the known Eu^{3+}-EDTA complex structure

Our optimized $[Eu^{3+}\text{-}EDTA^{4-}\cdot(H_2O)_3]^-$ complex structure matches the coordination structure previously resolved with X-ray crystallography[68], where the Eu^{3+} ion is 9-coordinate with 4 oxygen atoms from the coordinated monodentate carboxylates, two nitrogen atoms from the

coordinated amines, and 3 oxygen atoms from the coordinated water molecules. This confirms that our Eu pseudopotential and basis set, as well as the AIMD protocol described, accurately replicate the structure of the $[Eu^{3+}\text{-}EDTA^{4-}\cdot(H_2O)_3]^-$ complex in solution, in which the EDTA protonation states correspond to pH 11.

Figure 2 shows the resulting optimized structure, with coordination sites 1, 2, and 3 corresponding to water molecules, coordination sites 4, 5, 8 and 9 to monodentate $-COO^-$ groups, and coordination sites 6 and 7 to amines. The atomic cartesian coordinates of the optimized $[Eu^{3+}\text{-}EDTA^{4-}\cdot(H_2O)_3]^-$ structure is reported in the SI.

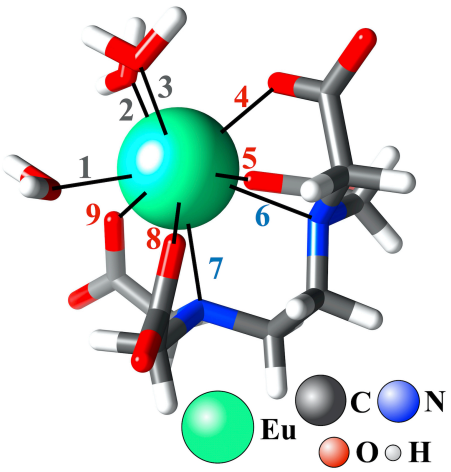

Figure 2. Geometry of the PBE/LnPP1 GTH optimized structure of the $[Eu^{3+}\text{-}EDTA^{4-}\cdot(H_2O)_3]^-$ complex. Black solid lines connected to the Eu atom demonstrate the positions of coordination sites. Coordination sites numbers colored in dark grey, red and blue represent water, monodentate $-COO^-$, and nitrogen atom coordination sites, respectively. Only water molecules coordinated to Eu^{3+} are shown for clarity.

From ~10 ps of equilibrated AIMD simulations of the $[Eu^{3+}\text{-}EDTA^{4-}\cdot(H_2O)_3]^-$ complex we calculated Eu-O (Figure 3a), Eu-N (Figure 3b), and Eu-C (Figure 3c) RDFs and CNs to quantify meaningful solution structures that account for ligand and solvent fluctuations, as well as to directly compare with reported Eu-O, Eu-N, and Eu-C distances measured with extended X-ray absorption fine structure (EXAFS) spectroscopy. Potential energy plot for corresponding AIMD trajectory is reported in Figure S1a in the SI.

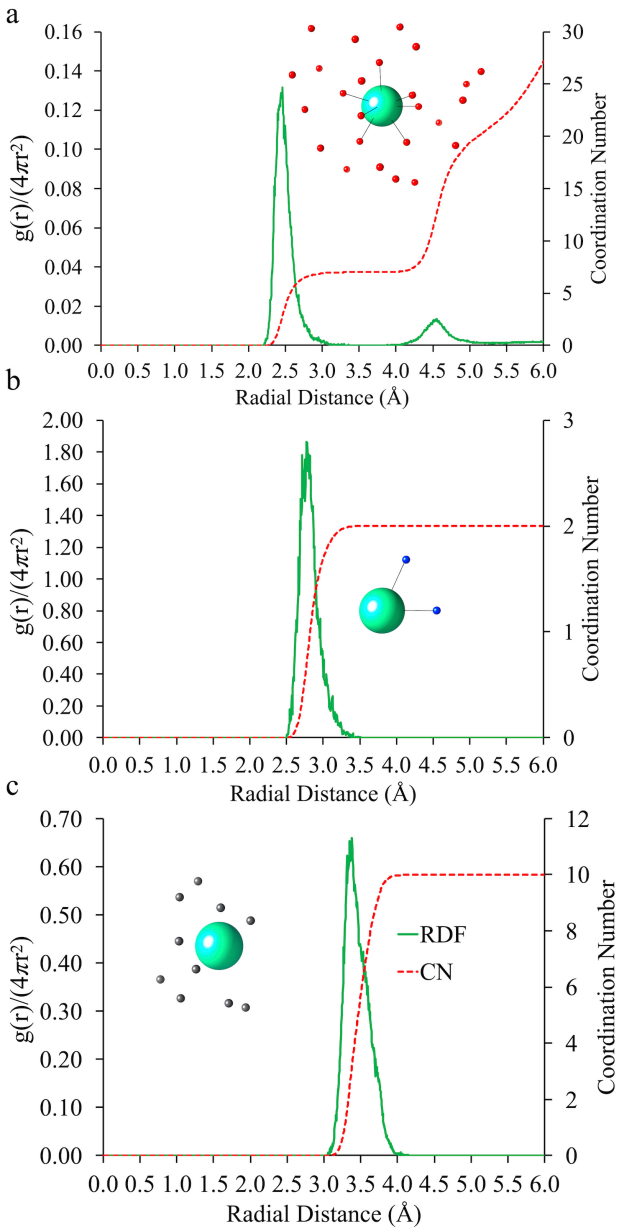

Figure 3. Radial distribution functions (RDF) and coordination numbers (CN) of the $[Eu^{3+}\text{-}EDTA^{4-}\cdot(H_2O)_3]^-$ complex from the equilibrated AIMD trajectory for a) Eu-O atoms, b) Eu-N atoms, and c) Eu-C atoms. Panels inside the graphs represent the distribution of the corresponding atoms in equilibrated and consecutively optimized structures. Solid lines connecting Eu with surrounding atoms represent coordinated atoms.

The RDFs calculated for the $[Eu^{3+}\text{-}EDTA^{4-}\cdot(H_2O)_3]^-$ complex, shown in Figure 3, have maxima at 2.46 Å for the Eu-O pair, 2.77 Å for the Eu-N pair, and 3.35 Å for the Eu-C pair. The oxygen and nitrogen atoms directly coordinated to the Eu^{3+} ion correspond to the first coordination sphere, with the ligand carbon atom slightly further away. In Figure 3a (Eu-O RDF)

a smaller peak at 4.57 Å is shown, which corresponds to the second coordination sphere, which is the solvent (water) shell around the $[Eu^{3+}\text{-}EDTA^{4-}\cdot(H_2O)_3]^-$ complex. The Eu-O and Eu-N RDFs we calculated from AIMD simulations closely match the previously EXAFS-measured Eu-O and Eu-N pair distances, reported as 2.41 Å and 2.76 Å, respectively.[69] Thus, the largest deviation between the experimentally measured radial pair distances and our calculated RDFs from AIMD simulations does not exceed 0.05 Å, demonstrating the reliability and accuracy of PBE/LnPP1 GTH AIMD simulations to replicate solution structures of Ln^{3+}-ligand complexes.

III.B. The solution structure of Eu^{3+}-nicotianamine complexes resolved with ab initio molecular dynamics

In order to account for different possible conformations of $[Eu^{3+}\text{-}NA]^{3+}$ complexes, we performed AIMD simulations of this system with three different initial conformations, as described in the computational section. We found two stable $[Eu^{3+}\text{-}NA]^{3+}$ complex structures. One structure includes three water molecules directly coordinated to the Eu^{3+} ion (Figure 4a), in which the Eu^{3+} ion is coordinated to two carboxylates in a bidentate conformation and one in a monodentate conformation. In the $[Eu^{3+}\text{-}NA\cdot(H_2O)_3]^{3+}$ complex structure (Figure 4a), coordination sites 1, 2, and 3 correspond to water molecules, coordination sites 4, 5, 7 and 8 to bidentate $-COO^-$ groups, and coordination site 6 to a monodentate $-COO^-$ group. The other structure has four water molecules directly coordinated to the Eu^{3+} ion (Figure 4b), in which the Eu^{3+} ion is coordinated to one carboxylate in a bidentate and two in a monodentate fashion. In the $[Eu^{3+}\text{-}NA\cdot(H_2O)_4]^{3+}$ complex structure (Figure 4b), coordination sites 1, 2, 3 and 4 correspond to water molecules, coordination sites 5 and 7 to the bidentate $-COO^-$ group, and coordination sites 6 and 8 two each monodentate $-COO^-$ group. The atomic cartesian coordinates of both complexes appear in the SI. Unlike the 9-coordinate $[Eu^{3+}\text{-}EDTA^{4-}\cdot(H_2O)_3]^-$ complex, both Eu-NA complexes are 8-coordinate.

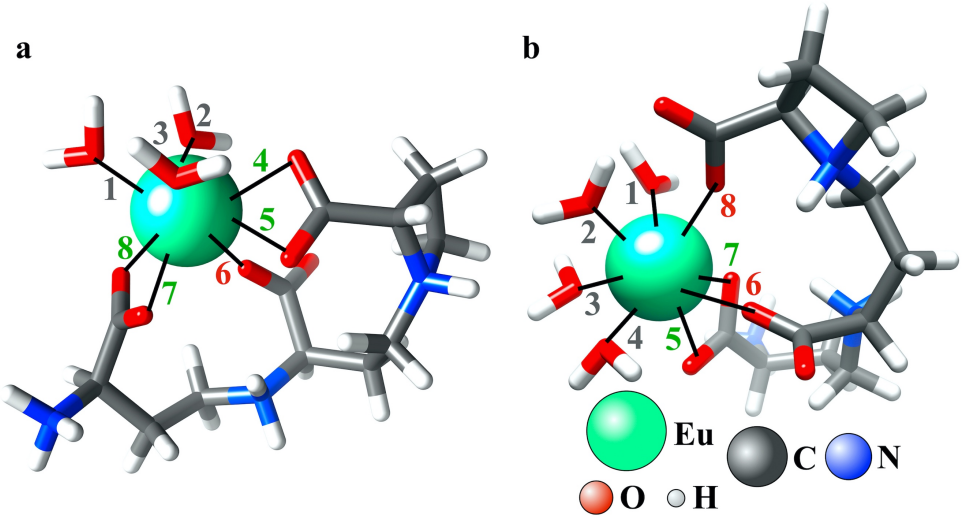

Figure 4. PBE/LnPP1 GTH geometry optimized structure of the a) $[Eu^{3+}\text{-}NA\cdot(H_2O)_3]^{3+}$ and b) $[Eu^{3+}\text{-}NA\cdot(H_2O)_4]^{3+}$ complexes. Black solid lines connected to Eu atom demonstrate the positions of coordination sites. Numbers colored in dark grey, red and green represent water, monodentate $-COO^-$, and bidentate $-COO^-$ coordination sites, respectively. Only water molecules coordinated to Eu^{3+} shown for clarity.

Starting from the optimized complex structures, we calculated the RDFs and CNs for both complexes using ~10 ps of equilibrated AIMD trajectories. Figures 5 and 6 show the Eu-O, Eu-N, and Eu-C RDFs and CNs of the $[Eu^{3+}\text{-}NA\cdot(H_2O)_3]^{3+}$ and $[Eu^{3+}\text{-}NA\cdot(H_2O)_4]^{3+}$ complexes respectively. Potential energy plots of the corresponding AIMD trajectories are reported in Figures S1b and S1c in the SI.

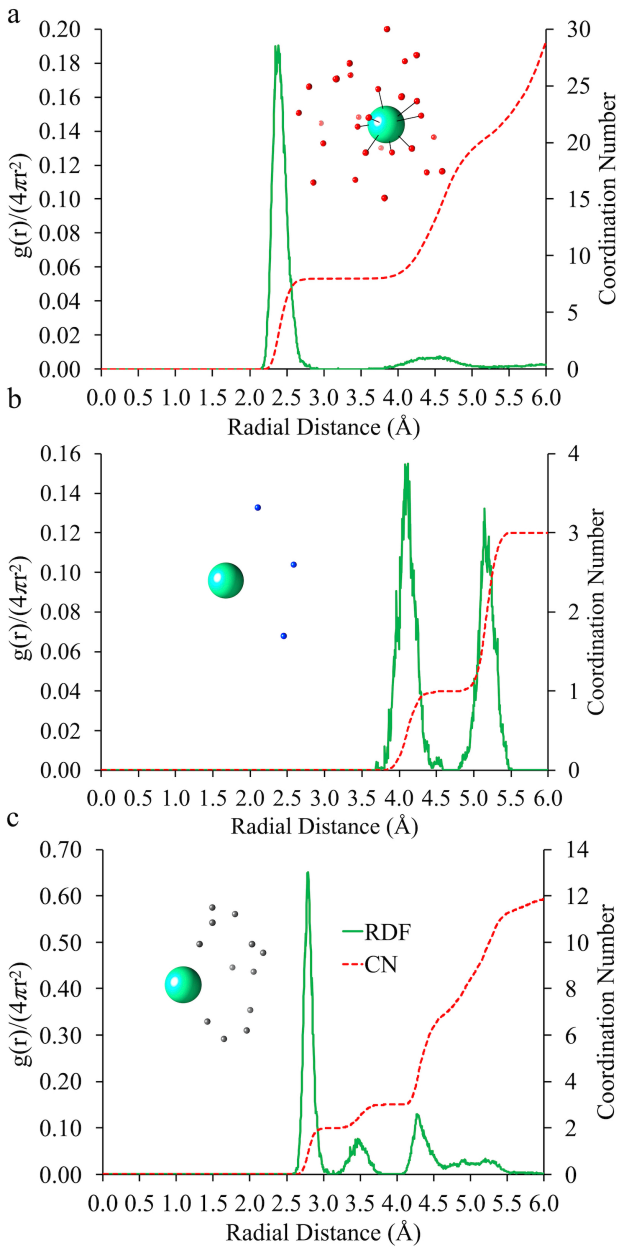

Figure 5. Radial distribution functions (RDF) and coordination numbers (CN) of the $[Eu^{3+}\text{-}NA\cdot(H_2O)_3]^{3+}$ complex from its equilibrated AIMD trajectory for a) Eu-O atoms, b) Eu-N atoms, and c) Eu-C atoms. Panels inside the graphs represent the distribution of the corresponding atoms in equilibrated and consecutively optimized structures. Solid lines connecting Eu atom and surrounding atoms represent coordinated atoms.

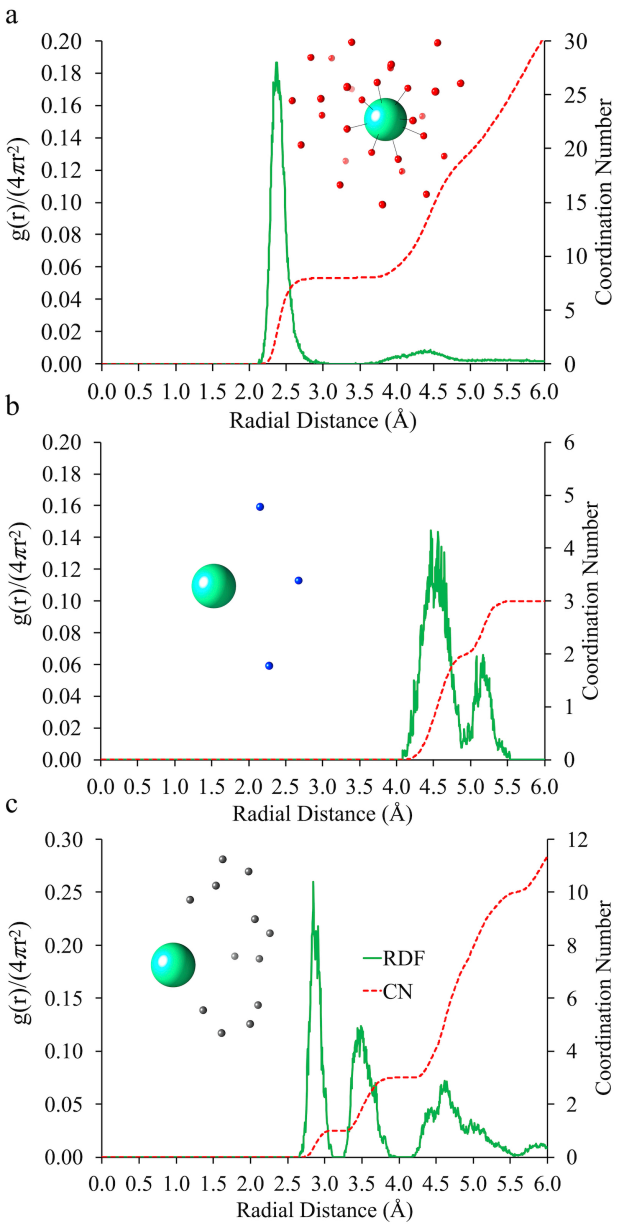

Figure 6. Radial distribution functions (RDF) and coordination numbers (CN) of the $[Eu^{3+}\text{-}NA\cdot(H_2O)_4]^{3+}$ complex from its equilibrated AIMD trajectory for a) Eu-O atoms, b) Eu-N atoms, and c) Eu-C atoms. Panels inside the graphs represent the distribution of the corresponding atoms in equilibrated and consecutively optimized structures. Solid lines connecting Eu atom and surrounding atoms represent coordinated atoms.

Table 1 shows the distances of the RDFs peaks, extracted from Figures 3, 5, and 6 to compare both $[Eu^{3+}\text{-}NA\cdot(H_2O)_n]^{3+}$ complex structures with each other and with the known $[Eu^{3+}\text{-}EDTA^{4-}\cdot(H_2O)_3]^{-}$ structure. Both 8-coordinate $[Eu^{3+}\text{-}NA\cdot(H_2O)_n]^{3+}$ complex structures are similar. Although both Eu-O RDF profiles closely match, there are subtle changes in the Eu-N

and Eu-C profiles. This means that the change in the binding mode of one carboxylate group from bidentate $[Eu^{3+}\text{-}NA\cdot(H_2O)_3]^{3+}$ to monodentate $[Eu^{3+}\text{-}NA\cdot(H_2O)_4]^{3+}$ resulted in a different solution structure for the entire complex, not only the carboxylate moiety.

Table 1. RDFs peaks for $[Eu^{3+}\text{-}EDTA^{4-}\cdot(H_2O)_3]^{-}$ and $[Eu^{3+}\text{-}NA\cdot(H_2O)_n]^{3+}$ complexes. Peak values are in Å. The peaks absent in RDFs marked with a "--".

	$[Eu^{3+}\text{-}EDTA^{4-}\cdot(H_2O)_3]^{-}$			$[Eu^{3+}\text{-}NA\cdot(H_2O)_3]^{3+}$			$[Eu^{3+}\text{-}NA\cdot(H_2O)_4]^{3+}$		
	1st	2nd	3rd	1st	2nd	3rd	1st	2nd	3rd
Eu-O	2.46	4.57	--	2.38	4.57	--	2.38	4.45	--
Eu-N	2.78	--	--	4.08	5.14	--	4.46	5.16	--
Eu-C	3.38	--	--	2.79	3.49	4.27	2.84	3.49	4.65

All three complexes share similar 1st (~2.4 Å) and 2nd (~4.5 Å) sphere Eu-O distances. While the $[Eu^{3+}\text{-}EDTA^{4-}\cdot(H_2O)_3]^{-}$ complex includes nitrogen atoms (amine sites) in its first coordination sphere, both $[Eu^{3+}\text{-}NA\cdot(H_2O)_n]^{3+}$ complexes have only oxygen atoms in their first solvation shell. This is evidenced in the Eu-N RDF plots, which show a single peak for $[Eu^{3+}\text{-}EDTA^{4-}\cdot(H_2O)_3]^{-}$ ~2.8 Å (Figure 3b), while more disordered peaks are seen for the $[Eu^{3+}\text{-}NA\cdot(H_2O)_n]^{3+}$ complexes at distances >4 Å (Figures 5b, 6b). This means that the amine NA sites are on the "outside" of the first coordination sphere of both Eu-NA complexes and in contact with solvent molecules, unlike the $[Eu^{3+}\text{-}EDTA^{4-}\cdot(H_2O)_3]^{-}$ complex structure where most heteroatoms are coordinated to the Eu^{3+} ion. Similarly, the Eu-C RDF plots of the $[Eu^{3+}\text{-}NA\cdot(H_2O)_n]^{3+}$ complexes are more disordered than the single Eu-C peak for $[Eu^{3+}\text{-}EDTA^{4-}\cdot(H_2O)_3]^{-}$, which implies that the $[Eu^{3+}\text{-}EDTA^{4-}\cdot(H_2O)_3]^{-}$ complex is more rigid than both $[Eu^{3+}\text{-}NA\cdot(H_2O)_n]^{3+}$ complexes. This has implications toward lanthanide-ligand complex stability and solubility.

III.C. Eu^{3+}coordination changes in the presence of nicotianamine

Ln^{3+} ions emit light,[4] a property we will use to determine Ln^{3+}-ligand complex formation, and which arises from transitions within the 4*f* orbitals. These ions form mostly ionic bonds that, along with their core nature, leave the 4*f* orbitals substantially unaffected by the coordination environment. While *f-f* transitions are forbidden by the parity rule, the symmetry of the

coordination environment partially lifts the restrictions, which enables the use of emission spectroscopy to characterize the symmetry of the coordination sphere of Eu^{3+}.[83] Excitation and emission spectra are easily interpreted for the Eu^{3+} ion, because it has a simple electronic structure in which the excited- and ground-state energy level multiplets do not overlap,[84] allowing for simple spectral interpretation. The fine structure in the emission spectra of Eu^{3+} complexes is directly related to the coordination sphere around Eu^{3+} and its symmetry.[85] Additionally, since the gap between the emissive and the ground electronic states of the ion is relatively narrow, the emission can be partially quenched by the presence of oscillators, such as OH functional groups. Excited state lifetimes in water and D_2O can be used to evaluate the number of oscillators in the coordination sphere of Eu.[82,86]

When Eu^{3+} complexes are excited at 395 nm into the $^7F_0 \rightarrow {}^5L_6$ transition of Eu^{3+}, the characteristic line-like emission spectrum of the metal ion is seen (Figure 7). Different coordination environments lead to slight changes in symmetry and thus fine structure, as can be seen from the spectra in Figure 7, which indicates that different species are obtained when EDTA coordinates to Eu^{3+} in different protonation states (i.e. different pH values). Figure 7 shows that the coordination environment of Eu^{3+} changed when in contact with EDTA, which agrees with the known fact that EDTA bind Eu^{3+}, and validates our experimental approach.

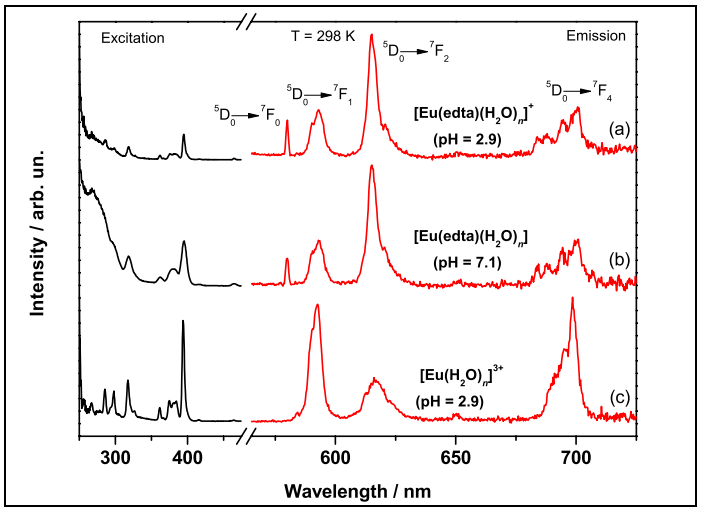

Figure 7. Excitation (black line, left) and emission (red line, right) spectra of (a) $[Eu^{3+}\text{-}EDTA^{2-}\cdot(H_2O)_n]^+$ at pH ~2.9, (b) $[Eu^{3+}\text{-}EDTA^{3-}\cdot(H_2O)_n]$ at pH ~7.1, and (c) $[Eu^{3+}\cdot(H_2O)_n]^{3+}$ complexes in aqueous solution. λ_{exc} = 395 nm.

Figure 8 shows that the coordination environment of Eu^{3+} changed when in contact with nicotianamine. The differences in emission and excitation curves between $[Eu^{3+}\cdot(H_2O)_n]^{3+}$ and $[Eu^{3+}\text{-}NA\cdot(H_2O)_n]^{3+}$ strongly suggest that Eu and NA are forming a complex because similar differences are observed when Eu^{3+} comes in contact with EDTA, which are known to form complexes. This supports, yet doesn't confirm, that nicotianamine binds Eu^{3+}, as predicted by computation. (Section III.B).

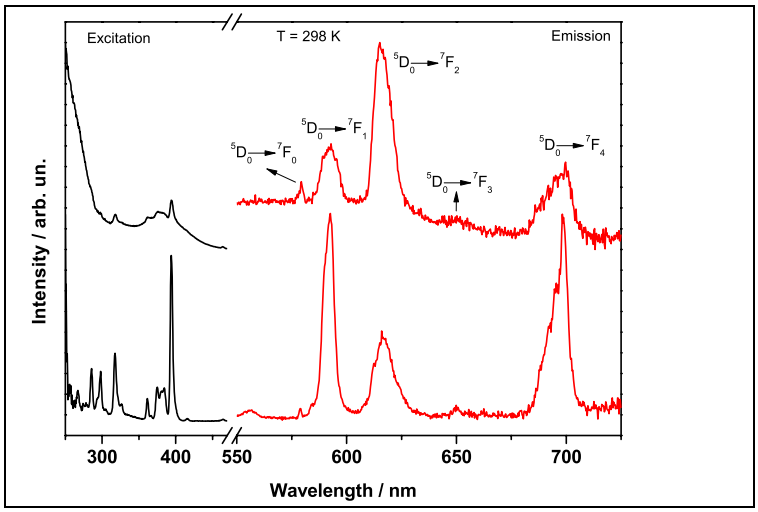

Figure 8. Excitation (black line, left) and emission (red line, right) spectra of $[Eu^{3+}\text{-}NA\cdot(H_2O)_n]^{3+}$ at pH ~4.8 (top, λ_{exc} = 260 nm) and $[Eu\cdot(H_2O)_n]^{3+}$ (bottom, λ_{exc} = 395 nm) complexes in aqueous solution.

III.D. Electronic structure of Eu^{3+}-ligand complexes

To spatially elucidate differences in the electronic properties of the Eu^{3+}-ligand complexes, we analyzed their electron density differences between bound and unbound states. Electron densities were calculated with PBE/ECP28MWBSEG//cc-pVTZ level of theory, as described in Section II.A.2. Electron density differences of the $[Eu^{3+}\text{-}EDTA^{4-}\cdot(H_2O)_3]^{-}$, $[Eu^{3+}\text{-}NA\cdot(H_2O)_3]^{3+}$, and $[Eu^{3+}\text{-}NA\cdot(H_2O)_4]^{3+}$ complexes are represented in Figures 9a, 9b and 9c, respectively.

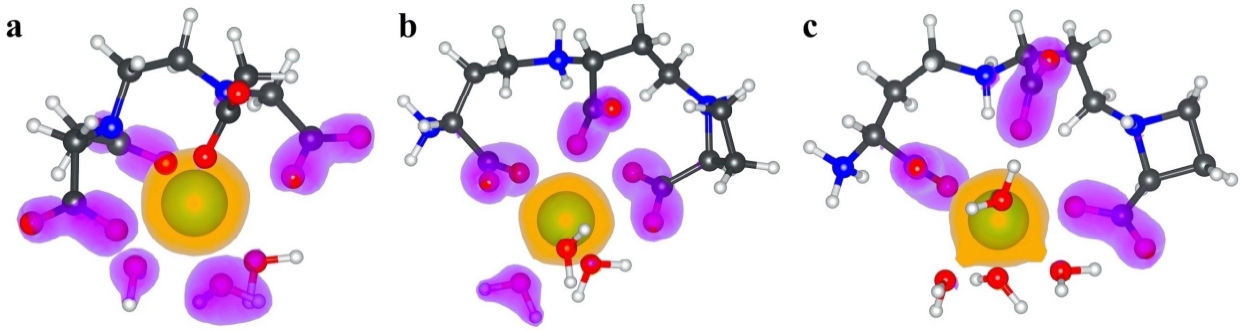

Figure 9. Electron density differences upon binding for a) $[Eu^{3+}\text{-}EDTA^{4-}\cdot(H_2O)_3]^-$, b) $[Eu^{3+}\text{-}NA\cdot(H_2O)_3]^{3+}$, and c) $[Eu^{3+}\text{-}NA\cdot(H_2O)_4]^{3+}$. Orange and purple colors represent net gain and net depletion of electronic density, respectively.

Figure 9a shows that, although the Eu^{3+} ion is coordinated to both nitrogen and oxygen atoms in the $[Eu^{3+}\text{-}EDTA^{4-}\cdot(H_2O)_3]^-$ complex, the main change in ligand electronic density is observed at $-COO^-$ coordination sites. Three out of four monodentate $-COO^-$ groups of the $[Eu^{3+}\text{-}EDTA^{4-}\cdot(H_2O)_3]^-$ complex display a substantial change in electronic density upon binding. It is unlikely that the particular $-COO^-$ group in Figure 9a without a net electron density gain always remains so. Most likely, the time-averaged behavior is that three of four EDTA carboxylate groups are more tightly bound to the Eu^{3+} ion than the fourth one, although the specific carboxylate groups displaying this behavior changes over time due to the dynamic nature of solution structures. This is shown from analysis of $Eu^{3+}\text{-}O_{carboxylate}$ bond distances along the AIMD trajectory of the $[Eu^{3+}\text{-}EDTA^{4-}\cdot(H_2O)_3]^-$ complex (Figure S3a), which reveals the distance's dynamics. Bond lengths vary between ~2.30 and ~2.70 Å. In most frames during the trajectory the distance of one carboxylate group is further from Eu^{3+} that the remaining three. Therefore, the observation that a $-COO^-$ group has no significant electron density loss (Figure 9a), is partly due to the fact that it is further from the remaining three in that particular optimized frame. Due to steric clashes and the coordination geometry around Eu^{3+} ions, not all $Eu\text{-}O_{carboxylate}$ bond distances will be equal, and they will vary in the solution phase.

Both $[Eu^{3+}\text{-}NA\cdot(H_2O)_n]^{3+}$ complexes in Figures 9b and 9c show all their carboxylate sites having a net gain loss of electronic density upon binding. This agrees with the Eu-O RDF values in Table 1, which shows the Eu-O RDF at 2.38 Å for both $[Eu^{3+}\text{-}NA\cdot(H_2O)_n]^{3+}$ complexes, while 2.46 Å for the Eu-O RDF of the $[Eu^{3+}\text{-}EDTA^{4-}\cdot(H_2O)_3]^-$ complex. This could be due that, unlike EDTA, NA only uses $-COO^-$ to bind the Eu^{3+} ion, and without the amine contribution the

carboxylates play a larger role. Alternatively, the shorter Eu-O distances in the NA complexes could be due to the fact that both $[Eu^{3+}\text{-}NA\cdot(H_2O)_n]^{3+}$ complexes are 8-coordinate while the $[Eu^{3+}\text{-}EDTA^{4-}\cdot(H_2O)_3]^{-}$ complex is 9-coordinate, leaving less steric clashes in the $[Eu^{3+}\text{-}NA\cdot(H_2O)_n]^{3+}$ complexes, resulting in that the carboxylate groups remain closer to the Eu^{3+} ion than those in the EDTA complex. For $[Eu^{3+}\text{-}NA\cdot(H_2O)_n]^{3+}$ complexes, Figures S3b and S3c show Eu-$O_{carboxylate}$ bond distances for monodentate -$OCOO^{-}$ groups and Figures S4b and S4c show Eu-$O_{carboxylate}$ bond distances for bidentate -$OCOO^{-}$ groups. Coordination bond lengths with monodentate carboxylates in NA ligands (vary between ~2.20 and ~2.40 Å) are closer than those in the EDTA complex. However, Eu-$O_{carboxylate}$ bond distances for bidentate -$OCOO^{-}$ groups are longer (vary between ~2.30 to ~2.80), suggesting that coordination bond length is not the only contributor to net electron density loss in a coordinating functional group.

All complexes have water molecules coordinated to the Eu^{3+} ion, however the $[Eu^{3+}\text{-}EDTA^{4-}\cdot(H_2O)_3]^{-}$ complex has two water molecules with a significant net loss of electron density (Figure 9a), the $[Eu^{3+}\text{-}NA\cdot(H_2O)_3]^{3+}$ complex has one water molecule a significant net loss of electron density (Figure 9b), and the $Eu^{3+}\text{-}NA\cdot(H_2O)_4]^{3+}$ complex no bound water molecule with a significant net loss of electron density (Figure 9a). This indicates a higher contribution of water molecules to binding in the $[Eu^{3+}\text{-}EDTA^{4-}\cdot(H_2O)_3]^{-}$ than the $[Eu^{3+}\text{-}NA\cdot(H_2O)_n]^{3+}$ complexes. Eu-O_{water} bond lengths along the AIMD trajectories for the $[Eu^{3+}\text{-}EDTA^{4-}\cdot(H_2O)_3]^{-}$ and $[Eu^{3+}\text{-}NA\cdot(H_2O)_n]^{3+}$ complexes (Figure S5) show longer coordination bond lengths in the EDTA complex. This suggests that net electron density loss in a coordinating functional group has multiple causes, and bond lengths alone are not predictive of which coordinating functional group will contribute electron density to bound ion.

To further investigate coordination bonds in $[Eu^{3+}\text{-}NA\cdot(H_2O)_n]^{3+}$ complexes, we analyzed their valence MOs, which were calculated with PBE/ECP28MWBSEG//cc-pVTZ level of theory. The MO diagrams for valence orbitals of $[Eu^{3+}\text{-}NA\cdot(H_2O)_3]^{3+}$ and $[Eu^{3+}\text{-}NA\cdot(H_2O)_4]^{3+}$ appear in Figure 10a, and a depiction of selected valence MOs are shown in Figure 10b. We focused on analysis of the valence orbitals rather than the electronic excitations, because, as shown in previous studies,[87,88] such analysis is sufficient to qualitatively elucidate coordination properties. TDDFT or multi-reference calculations are necessary for more robust quantitative validation of Ln^{3+} complexes stabilities;[32,89–92] however, in this work we focus on describing the structure of

the complexes, and we will quantify stabilities in the near future. Thus, in the present paper, we provide a qualitative description of the electronic structure of the previously unresolved Eu^{3+}-nicotianamine complexes to complement our molecular structure findings (Section III.B).

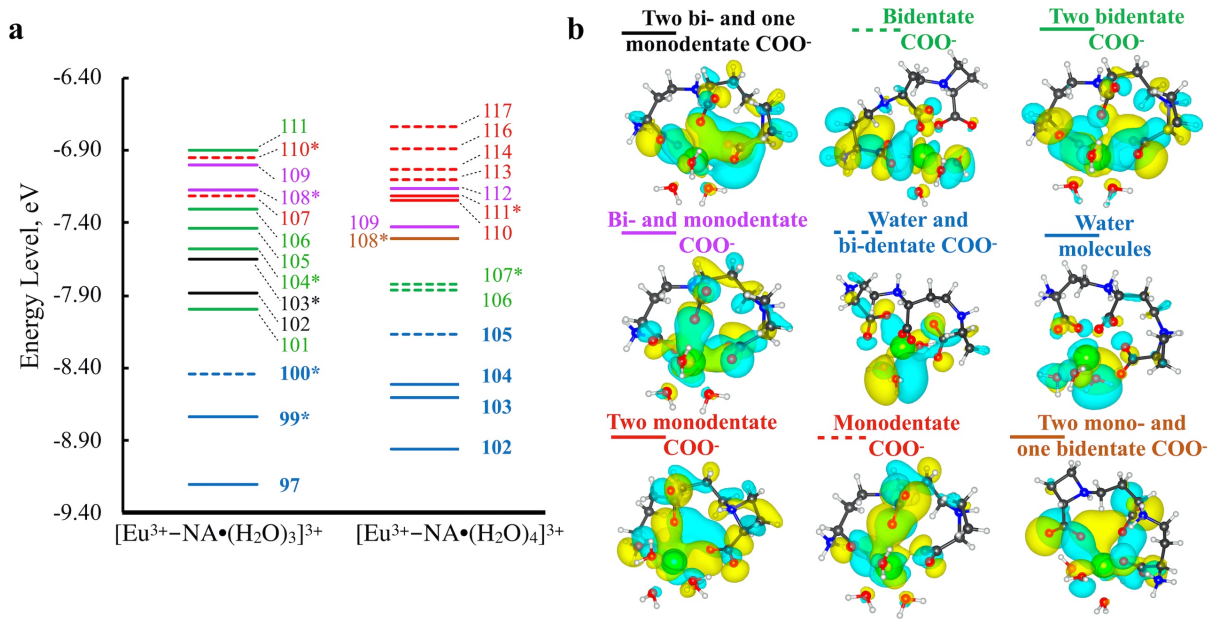

Figure 10. Valence MOs of $[Eu^{3+}\text{-}NA\cdot(H_2O)_3]^{3+}$ and $[Eu^{3+}\text{-}NA\cdot(H_2O)_4]^{3+}$ complexes. a) MO diagrams. The MOs marked with the "*" were selected for visualization of particular MO type. b) Representative MOs, the orbital wave functions are positive in the yellow regions and negative in the cyan. Different colors of orbital labels and solid or dashed lines indicate type of MO orbital. The notations next to MOs describe coordination sites with the dominant contributions to the given type of MO.

Figure 10a shows that the energy levels of MOs in the $[Eu^{3+}\text{-}NA\cdot(H_2O)_3]^{3+}$ complex are qualitatively different, and generally lower than those in the $[Eu^{3+}\text{-}NA\cdot(H_2O)_4]^{3+}$ complex. This indicates that having one carboxylate group change from bidentate ($[Eu^{3+}\text{-}NA\cdot(H_2O)_3]^{3+}$) to monodentate ($[Eu^{3+}\text{-}NA\cdot(H_2O)_4]^{3+}$) affects not only the number of bound water molecules, but also the electronic structure in all coordination bonds. Moreover, drastically lower energies of MOs corresponding to bound water molecules in the $[Eu^{3+}\text{-}NA\cdot(H_2O)_3]^{3+}$ complex compared to the bound water MOs in $[Eu^{3+}\text{-}NA\cdot(H_2O)_4]^{3+}$ complex, indicate that water molecules have higher contribution to binding in the $[Eu^{3+}\text{-}NA\cdot(H_2O)_3]^{3+}$ complex. This observation is consistent with net electron density loss in one water molecule in the $[Eu^{3+}\text{-}NA\cdot(H_2O)_3]^{3+}$ complex (Figure 9b) but not in the $[Eu^{3+}\text{-}NA\cdot(H_2O)_4]^{3+}$ (Figure 9c). Based on these observations, we hypothesize that

the $[Eu^{3+}\text{-}NA\cdot(H_2O)_3]^{3+}$ complex is more stable than $[Eu^{3+}\text{-}NA\cdot(H_2O)_4]^{3+}$, and nicotianamine will preferably bind Eu^{3+} with two bidentate and one monodentate carboxylate groups.

IV. Conclusions

This work shows that our pseudopotentials and basis sets with AIMD simulations can accurately predict the structure of lanthanide-ligand complexes in solution (i.e. in the condensed phase), by replicating the structure of the $[Eu^{3+}\text{-}EDTA^{4-}\cdot(H_2O)_3]^-$ complex in basic conditions within 0.05 Å, compared to X-ray fine structure absorption spectroscopy measurements from the literature.[68,69] Paired with the fact that our pseudopotentials and basis sets can accurately predict lanthanide reactivity,[58] a very powerful computational approach allows us to properly predict lanthanide structures and reactions in the condensed phase. This will be highly useful to efforts in rare earth separation and purification, lanthanide-ligand based medical contrast agents, single molecule magnets, luminescent molecules, and any field in which resolving the structure and reactivity of lanthanides in the atomic scale is relevant.

This work also reports two very similar Eu^{3+}-nicotianamine complex structures that were predicted using our computational approach, which is supported by the fact that the same computational methods and approach were used to replicate the known Eu^{3+}-EDTA structure. While our excitation and emission spectroscopy measurements by themselves do not resolve the structure, they confirm that the coordination sphere of the Eu^{3+} ions changes when in contact with nicotianamine, strongly supporting that the computationally predicted Eu^{3+}-nicotianamine complex is forming. The spatial distribution of electron density gain or loss shows that not all coordinating groups contribute to the electron density gain in the bound ion. Different binding modes (mono- or bidentate) of a single carboxylate changes the electronic properties of all complex coordination bonds. We are currently quantifying lanthanide-ligand complex stabilities and thermodynamics, and will report them in the near future. Although knowledge that nicotianamine binds europium does not determine how plants uptake rare earths from the environment, it strongly supports that phytosiderophores bind lanthanides.

Supporting Information: Atomic cartesian coordinates (Å) of the PBE/LnPP1 GTH optimized structures of $[Eu^{3+}\text{-}EDTA^{4-}\cdot(H_2O)_3]^-$, $[Eu^{3+}\text{-}NA\cdot(H_2O)_3]^{3+}$, and $[Eu^{3+}\text{-}NA\cdot(H_2O)_4]^{3+}$ complexes. Potential energy plots for AIMD trajectories of $[Eu^{3+}\text{-}EDTA^{4-}\cdot(H_2O)_3]^-$, $[Eu^{3+}\text{-}NA\cdot(H_2O)_3]^{3+}$, and $[Eu^{3+}\text{-}NA\cdot(H_2O)_4]^{3+}$ complexes. Coordination bond lengths of the $[Eu^{3+}\text{-}EDTA^{4-}\cdot(H_2O)_3]^-$, $[Eu^{3+}\text{-}NA\cdot(H_2O)_3]^{3+}$, and $[Eu^{3+}\text{-}NA\cdot(H_2O)_4]^{3+}$ complexes along the AIMD trajectories.

ORCID:

Danil S. Kaliakin: 0000-0002-9354-8248

Jorge H.S.K. Monteiro: 0000-0002-9622-3537

Ana de Bettencourt-Dias: 0000-0001-5162-2393

David C. Cantu: 0000-0001-9584-5062

Acknowledgments: This work was supported by Research and Innovation at the University of Nevada, Reno. Calculations were performed in Pronghorn, the High Performance Computing cluster of the University of Nevada, Reno. AdBD acknowledges NSF support of this work (CHE-1800392).

References

(1) Parker, D.; Williams, J. A. G. Getting Excited about Lanthanide Complexation Chemistry. *J. Chem. Soc. Dalt. Trans.* **1996**, 3613.

(2) Parker, D.; Dickins, R. S.; Puschmann, H.; Crossland, C.; Howard, J. A. K. Being Excited by Lanthanide Coordination Complexes: Aqua Species, Chirality, Excited-State Chemistry, and Exchange Dynamics. *Chem. Rev.* **2002**, *102*, 1977–2010.

(3) Bettinelli, M.; Carlos, L.; Liu, X. Lanthanide-Doped Upconversion Nanoparticles. *Phys. Today* **2015**, *68*, 38–44.

(4) *Luminescence of Lanthanide Ions in Coordination Compounds and Nanomaterials*; de Bettencourt-Dias, A., Ed.; John Wiley and Sons: Hoboken, 2014.

(5) Bünzli, J. C. G. Luminescence Bioimaging with Lanthanide Complexes. In *Luminescence of Lanthanide Ions in Coordination Compounds and Nanomaterials*; 2014; pp. 125–196.

(6) Deiters, E.; Song, B.; Chauvin, A. S.; Vandevyver, C. D. B.; Gumy, F.; Bünzli, J. C. G. Luminescent Bimetallic Lanthanide Bioprobes for Cellular Imaging with Excitation in the Visible-Light Range. *Chem. - A Eur. J.* **2009**, *15*, 885–900.

(7) Faulkner, S.; Pope, S. J. A.; Burton-Pye, B. P. Lanthanide Complexes for Luminescence Imaging Applications. *Appl. Spectrosc. Rev.* **2005**, *40*, 1–31.

(8) Jia, J. H.; Li, Q. W.; Chen, Y. C.; Liu, J. L.; Tong, M. L. Luminescent Single-Molecule Magnets Based on Lanthanides: Design Strategies, Recent Advances and Magneto-Luminescent Studies. *Coord. Chem. Rev.* **2019**, *378*, 365–381.
(9) *Lanthanide Probes in Life, Chemical and Earth Sciences Theory and Practice*; Bünzli, J.-C. G.; Choppin, G. R., Eds.; Elsevier Science Ltd: Amsterdam, Netherlands, 1990.
(10) Sastri, V. S.; Bünzli, J. C.; Rao, V. R.; Rayudu, G. V. S.; Perumareddi, J. R. *Modern Aspects of Rare Earths and Their Complexes*; Elsevier Science Ltd: Amsterdam, Netherlands, 2003.
(11) Cheisson, T.; Schelter, E. J. Rare Earth Elements: Mendeleev's Bane, Modern Marvels. *Science (80-.).* **2019**, *363*, 489–493.
(12) Daumann, L. J. Essential and Ubiquitous: The Emergence of Lanthanide Metallobiochemistry. *Angew. Chemie - Int. Ed.* **2019**, *58*, 12795–12802.
(13) Lim, S.; Franklin, S. J. Lanthanide-Binding Peptides and the Enzymes That Might Have Been. *Cell. Mol. Life Sci.* **2004**, *61*, 2184–2188.
(14) Hibi, Y.; Asai, K.; Arafuka, H.; Hamajima, M.; Iwama, T.; Kawai, K. Molecular Structure of La3+-Induced Methanol Dehydrogenase-like Protein in Methylobacterium Radiotolerans. *J. Biosci. Bioeng.* **2011**, *111*, 547–549.
(15) Fitriyanto, N. A.; Fushimi, M.; Matsunaga, M.; Pertiwiningrum, A.; Iwama, T.; Kawai, K. Molecular Structure and Gene Analysis of Ce3+-Induced Methanol Dehydrogenase of Bradyrhizobium Sp. MAFF211645. *J. Biosci. Bioeng.* **2011**, *111*, 613–617.
(16) Nakagawa, T.; Mitsui, R.; Tani, A.; Sasa, K.; Tashiro, S.; Iwama, T.; Hayakawa, T.; Kawai, K. A Catalytic Role of XoxF1 as La3+-Dependent Methanol Dehydrogenase in Methylobacterium Extorquens Strain AM1. *PLoS One* **2012**, *7*, 1–7.
(17) Tyler, G. Rare Earth Elements in Soil and Plant Systems - A Review. *Plant Soil* **2004**, *267*, 191–206.
(18) Ramírez-Olvera, S. M.; Trejo-Téllez, L. I.; García-Morales, S.; Pérez-Sato, J. A.; Gómez-Merino, F. C. Cerium Enhances Germination and Shoot Growth, and Alters Mineral Nutrient Concentration in Rice. *PLoS One* **2018**, *13*, 1–19.
(19) Cotruvo, J. A. The Chemistry of Lanthanides in Biology: Recent Discoveries, Emerging Principles, and Technological Applications. *ACS Cent. Sci.* **2019**, *5*, 1496–1506.
(20) Hider, R. C.; Yoshimura, E.; Khodr, H.; Wirén, N. Von; The, S.; Phytologist, N.; Nov, N. Competition or Complementation : The Iron-Chelating Abilities of Nicotianamine and Phytosiderophores. *New Phytol.* **2004**, *164*, 204–208.
(21) Ahmed, E.; Holmström, S. J. M. Siderophores in Environmental Research: Roles and Applications. *Microb. Biotechnol.* **2014**, *7*, 196–208.
(22) Ghosh, S. K.; Bera, T.; Chakrabarty, A. M. Microbial Siderophore - a Boon to Agricultural Sciences. *Biol. Control* **2020**, 104214.
(23) Leong, J. Siderophores: Their Biochemistry and Possible Role in the Biocontrol of Plant Pathogens. *Annu. Rev. Phytopathol.* **1986**, *24*, 187–209.
(24) Takahashi, M.; Terada, Y.; Nakai, I.; Nakanishi, H.; Yoshimura, E.; Mori, S.; Nishizawa,

N. K. Role of Nicotianamine in the Intracellular Delivery of Metals and Plant Reproductive Development. *Plant Cell* **2003**, *15*, 1263–1280.
(25) Ellis, R. J. Acid-Switched Eu(III) Coordination inside Reverse Aggregates: Insights into a Synergistic Liquid-Liquid Extraction System. *Inorganica Chim. Acta* **2017**, *460*, 159–164.
(26) Tircsó, G.; Garda, Z.; Kálmán, F. K.; Baranyai, Z.; Pócsi, I.; Balla, G.; Tóth, I. Lanthanide(III) Complexes of Some Natural Siderophores: A Thermodynamic, Kinetic and Relaxometric Study. *J. Inorg. Biochem.* **2013**, *127*, 53–61.
(27) Akbar, R.; Baral, M.; Kanungo, B. K. PH Dependent Photophysical Studies of New Europium and Terbium Complexes of Tripodal Ligand: Experimental and Semiempirical Approach. *J. Lumin.* **2015**, *167*, 27–44.
(28) Tei, L.; Baranyai, Z.; Brücher, E.; Cassino, C.; Demicheli, F.; Masciocchi, N.; Giovenzana, G. B.; Botta, M. Dramatic Increase of Selectivity for Heavy Lanthanide(III) Cations by Tuning the Flexibility of Polydentate Chelators. *Inorg. Chem.* **2010**, *49*, 616–625.
(29) Ellis, R. J.; Brigham, D. M.; Delmau, L.; Ivanov, A. S.; Williams, N. J.; Vo, M. N.; Reinhart, B.; Moyer, B. A.; Bryantsev, V. S. "Straining" to Separate the Rare Earths: How the Lanthanide Contraction Impacts Chelation by Diglycolamide Ligands. *Inorg. Chem.* **2017**, *56*, 1152–1160.
(30) Daumann, L. J.; Werther, P.; Ziegler, M. J.; Raymond, K. N. Siderophore Inspired Tetra- and Octadentate Antenna Ligands for Luminescent Eu(III) and Tb(III) Complexes. *J. Inorg. Biochem.* **2016**, *162*, 263–273.
(31) Kraemer, S. M.; Xu, J.; Raymond, K. N.; Sposito, G. Adsorption of Pb(II) and Eu(III) by Oxide Minerals in the Presence of Natural and Synthetic Hydroxamate Siderophores. *Environ. Sci. Technol.* **2002**, *36*, 1287–1291.
(32) Rohini; Baral, M.; Kanungo, B. K. Experimental and Theoretical Studies on Structure, Bonding and Luminescence Properties of Eu(III) and Tb(III) Complexes of a New Macrocyclic Based 8HQ Ligand. *J. Coord. Chem.* **2019**, *72*, 1497–1523.
(33) Abergel, R. J.; Warner, J. A.; Shuh, D. K.; Raymond, K. N. Enterobactin Protonation and Iron Release: Structural Characterization of the Salicylate Coordination Shift in Ferric Enterobactin. *J. Am. Chem. Soc.* **2006**, *128*, 8920–8931.
(34) Boiteau, R. M.; Shaw, J. B.; Pasa-Tolic, L.; Koppenaal, D. W.; Jansson, J. K. Micronutrient Metal Speciation Is Controlled by Competitive Organic Chelation in Grassland Soils. *Soil Biol. Biochem.* **2018**, *120*, 283–291.
(35) Von Wirén, N.; Klair, S.; Bansal, S.; Briat, J. F.; Khodr, H.; Shioiri, T.; Leigh, R. A.; Hider, R. C. Nicotianamine Chelates Both Fe(III) and Fe(II) Implications for Metal Transport in Plants. *Plant Physiol.* **1999**, *119*, 1107–1114.
(36) Von Wiren, N.; Khodr, H.; Hider, R. C. Hydroxylated Phytosiderophore Species Possess an Enhanced Chelate Stability and Affinity for Iron(III). *Plant Physiol.* **2000**, *124*, 1149–1157.
(37) Kovaříková, M.; Tomášková, I.; Soudek, P. Rare Earth Elements in Plants. *Biol. Plant.*

2019, *63*, 20–32.
(38) Poschenrieder, C.; Busoms, S.; Barceló, J. How Plants Handle Trivalent (+3) Elements. *Int. J. Mol. Sci.* **2019**, *20*, 1–25.
(39) Chistoserdova, L. Lanthanides: New Life Metals? *World J. Microbiol. Biotechnol.* **2016**, *32*, 1–7.
(40) Liu, C.; Hong, F. S.; Tao, Y.; Liu, T.; Xie, Y. N.; Xu, J. H.; Li, Z. R. The Mechanism of the Molecular Interaction between Cerium (III) and Ribulose-1,5-Bisphosphate Carboxylase/Oxygenase (Rubisco). *Biol. Trace Elem. Res.* **2011**, *143*, 1110–1120.
(41) Wildman, S. G. Along the Trail from Fraction I Protein to Rubisco (Ribulose Bisphosphate Carboxylase-Oxygenase). *Photosynth. Res.* **2002**, *73*, 243–250.
(42) Sharkey, T. D. Discovery of the Canonical Calvin–Benson Cycle. *Photosynth. Res.* **2019**, *140*, 235–252.
(43) Healy, M. R.; Ivanov, A. S.; Karslyan, Y.; Bryantsev, V. S.; Moyer, B. A.; Jansone-Popova, S. Efficient Separation of Light Lanthanides(III) by Using Bis-Lactam Phenanthroline Ligands. *Chem. - A Eur. J.* **2019**, *25*, 6326–6331.
(44) Clegg, S. L.; Zalupski, P. R.; Dutech, G. Ion Interaction Models and Measurements of Eu3+ Complexation: HEDTA in Aqueous Solutions at 25 °c Containing 1:1 Na+ Salts and Citrate PH Buffer. *Ind. Eng. Chem. Res.* **2016**, *55*, 2083–2096.
(45) Lumetta, G. J.; Rapko, B. M.; Garza, P. A.; Hay, B. P.; Gilbertson, R. D.; Weakley, T. J. R.; Hutchison, J. E. Deliberate Design of Ligand Architecture Yields Dramatic Enhancement of Metal Ion Affinity. *J. Am. Chem. Soc.* **2002**, *124*, 5644–5645.
(46) McCann, B. W.; Silva, N. De; Windus, T. L.; Gordon, M. S.; Moyer, B. A.; Bryantsev, V. S.; Hay, B. P. Computer-Aided Molecular Design of Bis-Phosphine Oxide Lanthanide Extractants. *Inorg. Chem.* **2016**, *55*, 5787–5803.
(47) Gullekson, B. J.; Breshears, A. T.; Brown, M. A.; Essner, J. B.; Baker, G. A.; Walensky, J. R.; Paulenova, A.; Gelis, A. V. Extraction of Water and Speciation of Trivalent Lanthanides and Americium in Organophosphorus Extractants. *Inorg. Chem.* **2016**, *55*, 12675–12685.
(48) Goedecker, S.; Teter, M. Separable Dual-Space Gaussian Pseudopotentials. *Phys. Rev. B - Condens. Matter Mater. Phys.* **1996**, *54*, 1703–1710.
(49) Hartwigsen, C.; Goedecker, S.; Hutter, J. Relativistic Separable Dual-Space Gaussian Pseudopotentials from H to Rn. *Phys. Rev. B* **1998**, *58*, 3641–3662.
(50) Krack, M. Pseudopotentials for H to Kr Optimized for Gradient-Corrected Exchange-Correlation Functionals. *Theor. Chem. Acc.* **2005**, *114*, 145–152.
(51) Lippert, G.; Hutter, J.; Parrinello, M. A Hybrid Gaussian and Plane Wave Density Functional Scheme. *Mol. Phys.* **1997**, *92*, 477–488.
(52) Cantu, D. C.; Lee, J.; Lee, M. S.; Heldebrant, D. J.; Koech, P. K.; Freeman, C. J.; Rousseau, R.; Glezakou, V. A. Dynamic Acid/Base Equilibrium in Single Component Switchable Ionic Liquids and Consequences on Viscosity. *J. Phys. Chem. Lett.* **2016**, *7*, 1646–1652.

(53) Lawson Daku, L. M. Spin-State Dependence of the Structural and Vibrational Properties of Solvated Iron(II) Polypyridyl Complexes from AIMD Simulations: Aqueous [Fe(Bpy)3]Cl2, a Case Study. *Phys. Chem. Chem. Phys.* **2018**, *20*, 6236–6253.
(54) Ruiz Pestana, L.; Mardirossian, N.; Head-Gordon, M.; Head-Gordon, T. Ab Initio Molecular Dynamics Simulations of Liquid Water Using High Quality Meta-GGA Functionals. *Chem. Sci.* **2017**, *8*, 3554–3565.
(55) Hahn, K. R.; Iannuzzi, M.; Seitsonen, A. P.; Hutter, J. Coverage Effect of the CO2 Adsorption Mechanisms on CeO 2(111) by First Principles Analysis. *J. Phys. Chem. C* **2013**, *117*, 1701–1711.
(56) Wang, Y. G.; Mei, D.; Li, J.; Rousseau, R. DFT+U Study on the Localized Electronic States and Their Potential Role during H2O Dissociation and CO Oxidation Processes on CeO 2(111) Surface. *J. Phys. Chem. C* **2013**, *117*, 23082–23089.
(57) Perdew, J. P.; Burke, K.; Ernzerhof, M. Generalized Gradient Approximation Made Simple. *Phys. Rev. Lett.* **1996**, *77*, 3865–3868.
(58) Lu, J. B.; Cantu, D. C.; Nguyen, M. T.; Li, J.; Glezakou, V. A.; Rousseau, R. Norm-Conserving Pseudopotentials and Basis Sets to Explore Lanthanide Chemistry in Complex Environments. *J. Chem. Theory Comput.* **2019**, *15*, 5987–5997.
(59) Cao, X.; Dolg, M. Valence Basis Sets for Relativistic Energy-Consistent Small-Core Lanthanide Pseudopotentials. *J. Chem. Phys.* **2001**, *115*, 7348–7355.
(60) Weigand, A.; Cao, X.; Yang, J.; Dolg, M. Quasirelativistic F-in-Core Pseudopotentials and Core-Polarization Potentials for Trivalent Actinides and Lanthanides: Molecular Test for Trifluorides. *Theor. Chem. Acc.* **2010**, *126*, 117–127.
(61) Ross, R. B.; Gayen, S.; Ermler, W. C. Ab Initio Relativistic Effective Potentials with Spin-Orbit Operators. V. Ce through Lu. *J. Chem. Phys.* **1994**, *100*, 8145–8155.
(62) Cundari, T. R.; Stevens, W. J. Effective Core Potential Methods for the Lanthanides. *J. Chem. Phys.* **1993**, *98*, 5555–5565.
(63) Hay, P. J.; Wadt, W. R. Ab Initio Effective Core Potentials for Molecular Calculations. Potentials for the Transition Metal Atoms Sc to Hg. *J. Chem. Phys.* **1985**, *82*, 270–283.
(64) Dolg, M.; Stoll, H. Pseudopotential Study of the Rare Earth Monohydrides, Monoxides and Monofluorides. *Theor. Chim. Acta* **1989**, *75*, 369–387.
(65) Dolg, M.; Stoll, H.; Preuss, H. Energy-Adjusted Ab Initio Pseudopotentials for the Rare Earth Elements. *J. Chem. Phys* **1989**, *90*, 1730–1734.
(66) Cao, X.; Zhang, J.; Weissmann, D.; Dolg, M.; Chen, X. Accurate Quantum Chemical Modelling of the Separation of Eu3+ from Am3+/Cm3+ by Liquid-Liquid Extraction with Cyanex272. *Phys. Chem. Chem. Phys.* **2015**, *17*, 20605–20616.
(67) Huang, P. W.; Wang, C. Z.; Wu, Q. Y.; Lan, J. H.; Song, G.; Chai, Z. F.; Shi, W. Q. Theoretical Studies on the Synergistic Extraction of Am3+ and Eu3+ with CMPO-HDEHP and CMPO-HEH[EHP] Systems. *Dalt. Trans.* **2018**, *47*, 5474–5482.
(68) Sakagami, N.; Yamada, Y.; Konno, T.; Okamoto, K. I. Crystal Structures and Stereochemical Properties of Lanthanide(III) Complexes with Ethylenediamine-

N,N,N′,N′-Tetraacetate. *Inorganica Chim. Acta* **1999**, *288*, 7–16.
(69) Mathur, J. N.; Thakur, P.; Dodge, C. J.; Francis, A. J.; Choppin, G. R. Coordination Modes in the Formation of the Ternary Am(III), Cm(III), and Eu(III) Complexes with EDTA and NTA: TRLFS, 13C NMR, EXAFS, and Thermodynamics of the Complexation. *Inorg. Chem.* **2006**, *45*, 8026–8035.
(70) Hutter, J.; Iannuzzi, M.; Schiffmann, F.; Vandevondele, J. Cp2k: Atomistic Simulations of Condensed Matter Systems. *Wiley Interdiscip. Rev. Comput. Mol. Sci.* **2014**, *4*, 15–25.
(71) VandeVondele, J.; Hutter, J. Gaussian Basis Sets for Accurate Calculations on Molecular Systems in Gas and Condensed Phases. *J. Chem. Phys.* **2007**, *127*.
(72) Grimme, S.; Antony, J.; Ehrlich, S.; Krieg, H. A Consistent and Accurate Ab Initio Parametrization of Density Functional Dispersion Correction (DFT-D) for the 94 Elements H-Pu. *J. Chem. Phys.* **2010**, *132*.
(73) Giard, A.; Filhol, J. S.; Jolibois, F.; Cavelier, F.; Berthomieu, D. Prediction of PKa Using DFT: The Nicotianamine Polyacid Example. *J. Chem. Theory Comput.* **2016**, *12*, 5493–5500.
(74) G., M. J. F.; Trucks, W.; Schlegel, H. B.; Scuseria, G. E.; Robb, M. A.; Cheeseman, J. R.; Scalmani, G.; A., V. B. G.; H., P.; Nakatsuji; et al. Gaussian. *Gaussian 09, Revis. A.01, Gaussian, Inc.* **2016**, 2016.
(75) Pritchard, B. P.; Altarawy, D.; Didier, B.; Gibson, T. D.; Windus, T. L. New Basis Set Exchange: An Open, Up-to-Date Resource for the Molecular Sciences Community. *J. Chem. Inf. Model.* **2019**, *59*, 4814–4820.
(76) Woon, D. E.; Dunning, T. H. Gaussian Basis Sets for Use in Correlated Molecular Calculations. I. The Atoms Boron through Neon and Hydrogen. *J. Chem. Phys.* **1988**, *90*, 1007–1023.
(77) Tomasi, J.; Mennucci, B.; Cammi, R. Quantum Mechanical Continuum Solvation Models. *Chem. Rev.* **2005**, *105*, 2999–3093.
(78) Miertuš, S.; Scrocco, E.; Tomasi, J. Electrostatic Interaction of a Solute with a Continuum. A Direct Utilizaion of AB Initio Molecular Potentials for the Prevision of Solvent Effects. *Chem. Phys.* **1981**, *55*, 117–129.
(79) Cossi, M.; Barone, V. Analytical Second Derivatives of the Free Energy in Solution by Polarizable Continuum Models. *J. Chem. Phys.* **1998**, *109*, 6246–6254.
(80) Cammi, R.; Tomasi, J. Remarks on the Use of the Apparent Surface Charges (ASC) Methods in Solvation Problems: Iterative versus Matrix-inversion Procedures and the Renormalization of the Apparent Charges. *J. Comput. Chem.* **1995**, *16*, 1449–1458.
(81) Nguyen, M. T.; Wang, Z.; Rod, K. A.; Childers, M. I.; Fernandez, C.; Koech, P. K.; Bennett, W. D.; Rousseau, R.; Glezakou, V. A. Atomic Origins of the Self-Healing Function in Cement-Polymer Composites. *ACS Appl. Mater. Interfaces* **2018**, *10*, 3011–3019.
(82) Supkowski, R. M.; Horrocks, W. D. W. On the Determination of the Number of Water Molecules, q, Coordinated to Europium(III) Ions in Solution from Luminescence Decay

Lifetimes. *Inorganica Chim. Acta* **2002**, *340*, 44–48.
(83) De Bettencourt-Dias, A. Introduction to Lanthanide Ion Luminescence. In *Luminescence of Lanthanide Ions in Coordination Compounds and Nanomaterials*; De Bettencourt-Dias, A., Ed.; John Wiley and Sons: Hoboken, 2014; p. 384.
(84) Dieke, G. H. *Spectra and Energy Levels of Rare Earth Ions in Crystals*; Interscience Publishers: New York, 1968.
(85) Tanner, P. A. *Lanthanide Luminescence in Solids*; Springer Ser. Fluoresc, 2011; Vol. 7.
(86) Morris, D. E. .; de Bettencourt-Dias, A. Spectroscopic Techniques and Instrumentation. In Luminescence of Lanthanide Ions in Coordination Compounds and Nanomaterials. In *Luminescence of Lanthanide Ions in Coordination Compounds and Nanomaterials*; de Bettencourt-Dias, A., Ed.; John Wiley and Sons: Hoboken, 2014; p. 384.
(87) Wang, C.; Wu, Q. Y.; Kong, X. H.; Wang, C. Z.; Lan, J. H.; Nie, C. M.; Chai, Z. F.; Shi, W. Q. Theoretical Insights into the Selective Extraction of Americium(III) over Europium(III) with Dithioamide-Based Ligands. *Inorg. Chem.* **2019**, *58*, 10047–10056.
(88) Ali, S. M. Role of Ligand Straining in Complexation of Eu3+-Am3+ Ions by TPEN and PPDEN, Scalar Relativistic DFT Exploration in Conjunction with COSMO-RS. *ACS Omega* **2018**, *3*, 13104–13116.
(89) Senegas, J. M.; Bernardinelli, G.; Imbert, D.; Bünzli, J. C. G.; Morgantini, P. Y.; Weber, J.; Piguet, C. Connecting Terminal Carboxylate Groups in Nine-Coordinate Lanthanide Podates: Consequences on the Thermodynamic, Structural, Electronic, and Photophysical Properties. *Inorg. Chem.* **2003**, *42*, 4680–4695.
(90) Emelina, T. B.; Freidzon, A. Y.; Bagaturyants, A. A.; Karasev, V. E. Electronic Structure and Energy Transfer in Europium(III)-Ciprofloxacin Complexes: A Theoretical Study. *J. Phys. Chem. A* **2016**, *120*, 7529–7537.
(91) Abbas, Z.; Dasari, S.; Beltrán-Leiva, M. J.; Cantero-López, P.; Páez-Hernández, D.; Arratia-Pérez, R.; Butcher, R. J.; Patra, A. K. Luminescent Europium(Iii) and Terbium(Iii) Complexes of β-Diketonate and Substituted Terpyridine Ligands: Synthesis, Crystal Structures and Elucidation of Energy Transfer Pathways. *New J. Chem.* **2019**, *43*, 15139–15152.
(92) Ardizzoia, G. A.; Colombo, G.; Therrien, B.; Brenna, S. Tuning the Fluorescence Emission and HOMO-LUMO Band Gap in Homoleptic Zinc(II) Complexes with N,O-Bidentate (Imidazo[1,5-a]Pyrid-3-Yl)Phenols. *Eur. J. Inorg. Chem.* **2019**, *2019*, 1825–1831.